Caving 2026 – A van As, D Cumming-Potvin & J Wesseloo (eds)

doi:10.36487/ACG_repo/2645_96

Estimating shaking and bulking ground velocities at Oyu Tolgoi mine

Erdenetogtokh Bayar [a,*], Bayarkhuu Batbayar [a], Ferric Mardiansyah [a], Zolzaya Bayartegsh [a], Denver Julian Birch [b]

[a] *Oyu Tolgoi, RioTinto, Mongolia*

[b] *Institute of Mine Seismology, Australia*

Abstract

Routine management of the seismic hazard at Oyu Tolgoi mine includes moment tensor analyses, which help to classify genuine seismic events into 2 main types: shear and crush. These correspond to 2 types of rock burst damage mechanisms – seismic shakedown and strain bursting – for which dynamic loading is quantified in terms of peak ground velocity (PGV) and strainburst velocity (V_{SB}), respectively. Using readily available information and software, we demonstrate appropriate methods for estimating PGV and V_{SB} from actual significant seismic events at Oyu Tolgoi mine. The results are compared with geotechnical observations, and an integration of these methods into the seismic hazard management plan is proposed.

Keywords: *rock mass deformation, ground motion, strainburst, peak ground velocity*

1 Introduction

Oyu Tolgoi is a porphyry copper–gold system comprising multiple orebodies, mined by open pit and underground methods. The mine is located in the Umnugobi province in the southern Gobi region of Mongolia. Figure 1a shows the location of the mine, and Figure 1b shows the distribution of mining areas across the orebodies. Mining at Oyu Tolgoi began at the Southern Oyu deposit with an open pit in 2010. At the same time, development of the underground mine proceeded in another part of the orebody system. Underground ore extraction alters the stress state of the surrounding rock mass, with mining at depths exceeding 1,300 m below surface contributing to the stress changes. Underground mining commenced in 2022 at Panel 0 (P0) and its surface breakthrough occurred in July 2025. During extraction of P0, rock mass stress conditions contributed to larger seismic events occurring in and around the cave footprint, particularly within zones of stiffer rock mass.

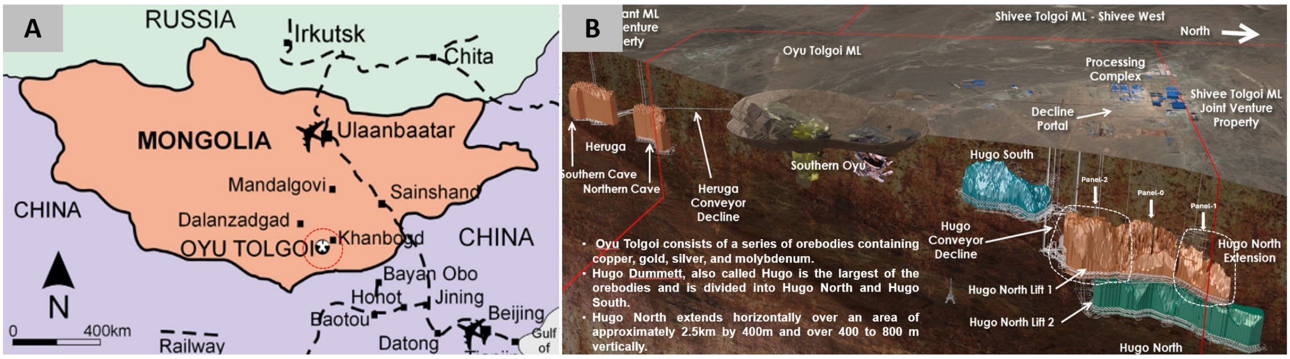

Figure 1 (a) Location of the mine property; (b) Orebodies at the Oyu Tolgoi mine site

There has been larger magnitude of the seismic events at the western perimeter of footprint. Specifically, there is apprehension about the potential for significant seismic events near the development face as well

* Corresponding author. Email address: erdenetogtokhb@ot.mn

as where the critical mine infrastructure is situated. The current risk management strategy involves implementing ground support that fully covers the excavation's skin as a minimum ground support measure during the development of the P0 cave. The western perimeter of the footprint is located mainly in the hanging wall sequence which is predominantly competent basalt with a uniaxial compressive strength of approximately 120 MPa. Different ground velocities must be considered when assessing the dynamic demand imposed on ground support for different types of rock burst (Figure 2).

- The velocity of ground motion associated with a seismic wave from a distant seismic event is relevant to the shakedown damage mechanism. The intensity of ground motion for this type of event can be quantified by the peak ground velocity (PGV).
- Velocity associated with the dynamic bulking of stress-fractured rock at the excavation perimeter is relevant to the strainburst damage mechanism. This is referred to as the bulking or strainbursting velocity (V_{SB}) (Malovichko et al. 2024).

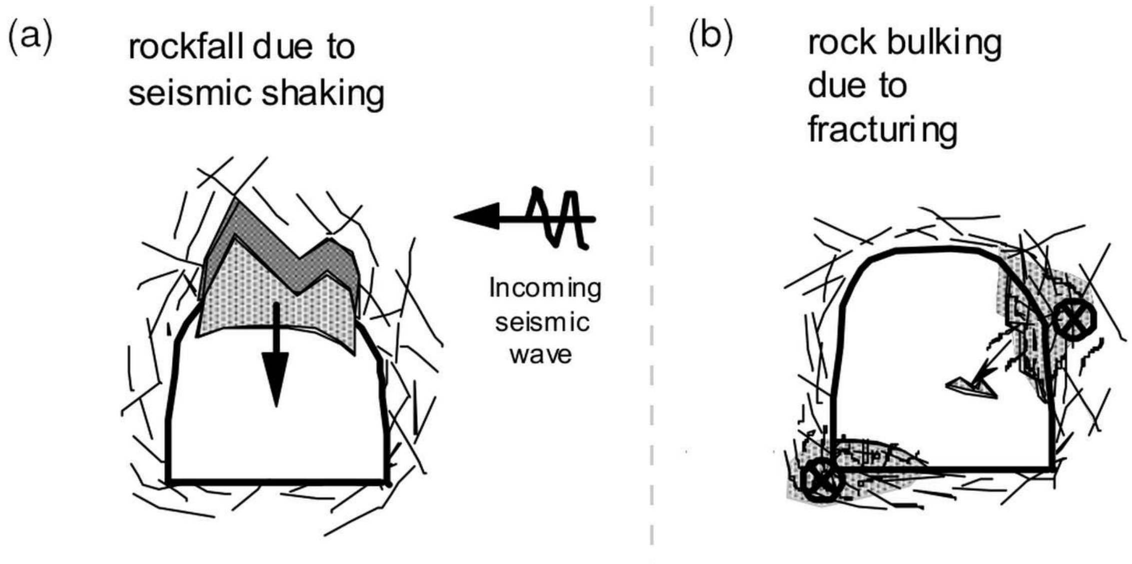

Figure 2 Two rock burst mechanisms described by Kaiser & Moss (2022). (a) Shakedown, which causes damage to an excavation or its support by a seismically induced fall of ground; (b) Strainburst, which is an excavation or support failure process whereby a highly stressed volume of unsupported or supported rock bursts near an excavation

Forecasting of both velocities for planned mining is discussed by Malovichko et al. (2024). This paper presents a retrospective forensic assessment of ground motions (PGV or V_{SB}, depending on the source type) for 3 large seismic events at Oyu Tolgoi and discusses the implications for ground control and seismic hazard management.

1.1 Geological setting of the Hugo North deposit

The mine sequence consists of folded Late Devonian units unconformably overlain by Carboniferous units. The Devonian sequence includes laminated siltstone, augite basalt and andesitic to dacitic ash-flow tuffs.

The Devonian sequence was intruded by multiple phases of large Devonian quartz monzodiorite (QMD) batholiths. Copper–gold mineralisation is spatially and temporarily related to the QMD intrusions. The Hugo North deposit hosts rocks are an east-dipping sequence of volcanic strata (Va) and QMD intrusive rocks. Stratigraphically, the lowest rocks in the sequence consist of basalt flows and minor Va overlain by an ignimbrite (IGN) sequence composed of dacite tuff and breccia. Figure 3 shows a plan and a cross-section of the geological model mapped at Hugo North, indicating the dominant lithological features and major geological structures. The distribution of the mineralised zones (concealed beneath a deformed sequence of Upper Devonian and Lower Carboniferous sedimentary and volcanic rocks) is strongly influenced by a protracted history of structural deformation (Lewis, 2003; 2004; Pope and Coombes, 2010)(Lewis, 2003; 2004; Pope and Coombes, 2010). These structures influence the distribution of mineralisation, including truncating and displacing lithological contacts, and has a significant impact on the rock mass quality.

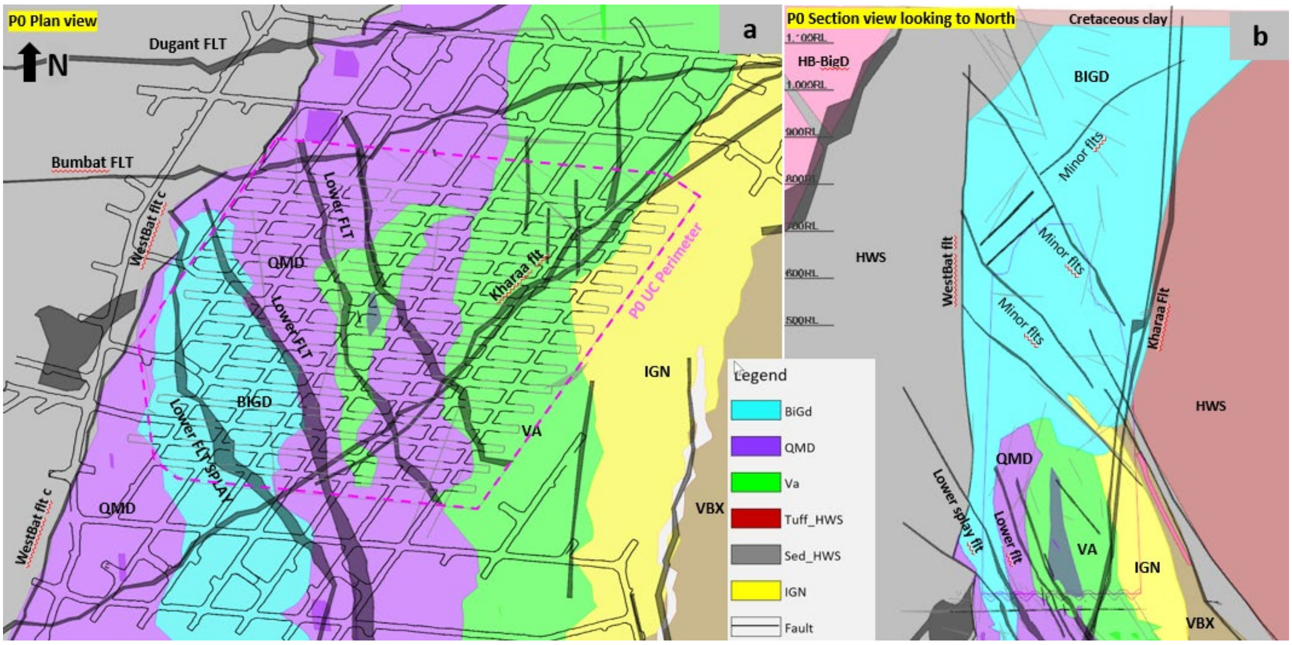

Figure 3 Geological model showing the major lithological features at Hugo North Lift 1. (a) Plan view; (b) Section view looking north

1.1.1 Faults and major structures

The Oyu Tolgoi deposit is underlain by a complex network of faults, folds and shear zones. Most of these structures are poorly exposed on the surface and have been defined through an integration of detailed exploration data (primarily drillhole and underground mapping data), property-scale geological mapping, and geophysical data. There is evidence for several phases of deformation and reactivation of the early faults during later deformational events. The West Bat Fault and mineralisation are displaced in a dextral shear sense towards the east, adjacent to the HbBiGd intrusion in Figure 3b. This displacement is controlled by the North Boundary Fault (NBF) system that broadly parallels the contact with the HbBiGd intrusion and consists of east to east-northeast striking faults. In terms of the rock mass response to mining, the higher magnitude events generally following the stiffer units separated by these structures (Figure 4).

1.1.2 Rock mass properties at Oyu Tolgoi

The rock mass properties at Oyu Tolgoi are typical of massive to moderately veined porphyry deposits. Much of the rock is moderately to heavily micro-defected such that the core often breaks easily when handled. Examination of drillcore suggests that many of the features logged as planar open joints might be counted more appropriately as irregular closed (healed) micro-defects that have opened up during the course of drilling. While stronger micro-defects tend to remain healed and uncounted as fractures (although their density is noted qualitatively), neighbouring, weaker micro-defects that have opened up appear to be regularly counted as open joints. Extensive laboratory testing has been undertaken to characterise the strength properties of the various dominant lithologies. SRK Consulting undertook a Hoek–Brown failure envelope regression on the testing and the results are tabulated in Table 1. The geotechnical properties of the different domains are primarily lithology and alteration.

Table 1 Geotechnical characterisation – P0 dominant rock mass properties (SRK Consulting 2022)

Lithology code (P0)	Alteration	Geotechnical domain	σci (avg.) (MPa)	σci (std.) (MPa)	σci (P_{50}) (MPa)	σci (P_{30}) (MPa)	m_i (avg.)	m_i (P_{50})
QMD	AAA	BGU04	55.7	16.7	55.7	46.9	16.0	16.0
BiGd	UNALT (low vein density)	BGU01a (LD)	115.9	21.4	113.9	103.5	12.3	12.1
Va-IGN contact	–	BGU16b	76.8	29.3	71.7	59.1	12.0	11.0
Va (DA1b)	AAA	BGU17	66.2	13,24	64.9	58.5	17.1	16.8

1.1.3 In situ stress regime

Several stress measurement have been conducted at Oyu Tolgoi, predominantly with overcoring using CSIRO's HI (hollow inclusion) stress cell in the exploration shafts and close to mining footprint. The current stress regime is divided into 3 different domains as a function of depth: a high horizontal stress (σ_1) trending 054°, a vertical stress consistent with the weight of the overburden (σ_2), and a low horizontal stress (σ_3) orthogonal to the other principal stresses. The magnitude of the stress field as a function of depth is listed in Tables 2 and 3 for Hugo North.

Table 2 Hugo North in situ stress gradient where z = depth below surface

Domain	Depth (m)	σ_1 (MPa)	σ_2 (MPa)	σ_3 (MPa)
1	0–600	0.047z	0.0265z	0.024z
2	600–800	0.071z – 13.95	0.0265z	0.027z – 1.59
3	>800	0.031z + 17.5	0.0265z	0.015z + 7.66

Table 3 Hugo North in situ stress at 1,300 m below surface

Principal stress	Magnitude (MPa)	Dip (°)	Bearing (°)
σ_1	57.8	00	055
σ_2	34.5	00	145
σ_3	27.2	90	–

1.2 Seismicity and damage observations

To date, seismic events with M_W ≥0.5 have predominantly occurred along the western perimeter and southwest of P0. This is largely attributed to variations in rock mass properties (a stiffness contrast) and stress partitioning across the West Bat Fault. Since monitoring began in 2018, strong rock mass response to development was almost exclusively limited to the stiffer units west of the West Bat Fault. In contrast, east of the footprint, rock mass behaviour is closer to ductile, and characterised by gradual tunnel deformation over time and due to mining of P0, with minimal occurrence of strong or dynamic responses to the mining. Figure 4 shows locations of large seismic events (M_W ≥0.5) at the mine. The locations of the primary crusher (PC1) and truck workshop (TWS) are marked for reference. The dominant source mechanism in the northwest is shear (where the largest seismic events are recorded) and crushing in the southwest near tunnels. Cave growth at P0 redistributes abutment stresses, contributing to damaging events near PC1 and TWS. Observations of damage along the western perimeter of P0 have been characterised as either the ejection of the tunnel support elements in the southwest or a combination of shear- and crush-type events that are stemming from the complex structure that exists at the northwest perimeter.

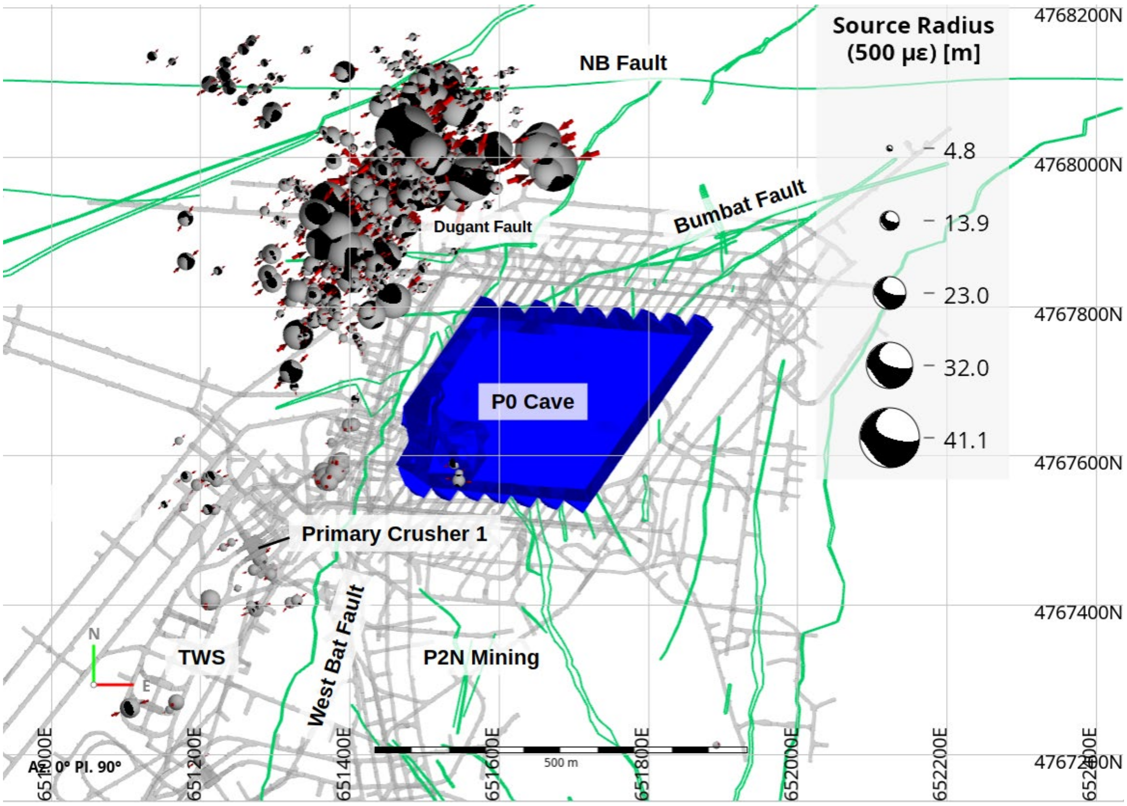

Figure 4 Plan view of locations of seismic events larger than M_W 0.5 around P0, mining block P2N and associated faults. The beach balls are sized according to the estimated source radius, assuming a constant average strain change over the source area of 5E^{-4}

2 Methodology

2.1 Estimating peak ground and near-fault velocity

Dynamic loading in the case of shakedown damage can be assessed using a ground motion prediction equation (GMPE), which describes the peak ground velocity as a function of seismic source strength (expressed in terms of a magnitude, seismic potency, P, or seismic energy) and the hypocentral distance R. Mendecki (2019) proposed a functional form of a GMPE suitable for mines as:

$$\overline{PGV} = PGV_0 \left[\frac{c_L \sqrt[3]{P}}{R + c_L \sqrt[3]{P}}\right]^{c_R} \quad (1)$$

where $\overline{PGV}$ is the expected mean value of peak ground velocity. This GMPE form suggests that the near-source peak ground velocity, PGV_0, is independent of event size. The coefficients c_L andc_R must be calibrated for the area of interest (e.g. in a part of the mine where damaging events occur). A method to estimate the near-fault peak ground velocity, PGV_0, is proposed by McGarr (1991). It is assumed that the strongest near-fault ground motion is associated with the rupture of a smaller part of the source (asperity), which produces the most intense velocity pulse in far-field waveforms. In an illustrative example shown in Figure 5, the total far-field velocity waveform (red) consists of the superposition of pulses from asperities 1 and 2 (blue and red, respectively), as well as radiation from the remaining parts of the fault r_0. The strongest far-field ground motion velocity is associated with the pulse from asperity 2.

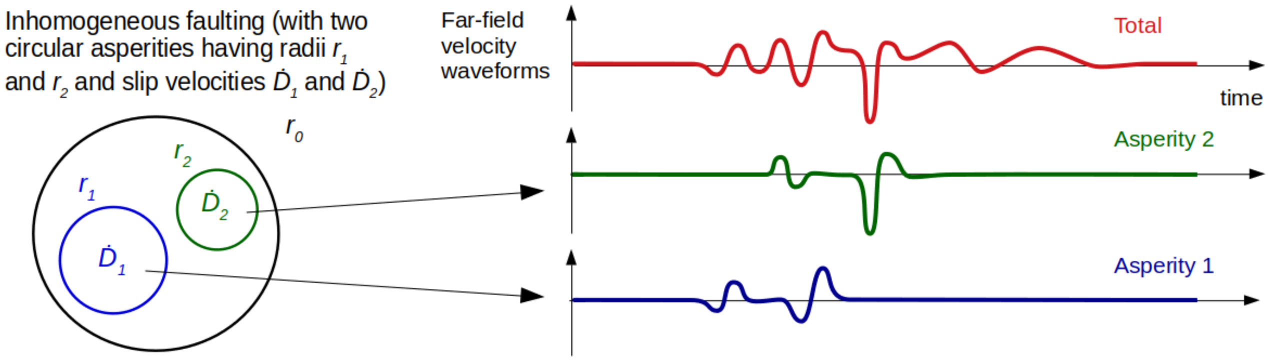

Figure 5 Schematic illustration of the contribution of fault asperities to the total far-field waveform

The maximum slip velocity is:

$$\dot{D} = 2.56 \left(\frac{\beta}{\mu}\right) \rho R a \quad (2)$$

where:

a	=	peak ground acceleration associated with the strongest velocity pulse
β	=	S-wave velocity
μ	=	shear modulus
ρ	=	rock mass density
R	=	hypocentral distance.

The maximum slip velocity ($\dot{D}$) represents the speed of relative motion of the fault, therefore the maximum near-fault velocity, PGV_0 in the vicinity of asperity 2 (Figure 5), is $\dot{D}/2$. An alternative approach is to evaluate the near-source PGV based on an effective stress σ_{eff} (i.e. the applied stress available to accelerate the 2 sides of the fault slip or shear failure source) as described by Mendecki (2019):

$$PGV_0 = 0.633 \frac{\sigma_{eff}}{\sqrt{\mu\rho}} \quad (3)$$

The uncertainty in input parameters, particularly PGV_0, should be considered when assessing the shakedown demand. The described approaches for evaluating PGV_0 apply to seismic sources representing fault slip or shear failure. Therefore, the assessment of dynamic loading using the presented GMPE is, strictly speaking, relevant only for slip-type seismic events. Malovichko (2023a) derived a calibrated GMPE for Oyu Tolgoi using the approach outlined by Mendecki (2019). In the initial calibration of the GMPE, the near-source ground motion was constrained by an average apparent S-wave velocity, β = 3,100 m/s and average strain change at source, $\Delta\epsilon = 1\text{E}^{-4}$. The fit with observed data took the form:

$$\overline{PGV} = 0.19530 \left[\frac{22.347\sqrt[3]{P}}{R+22.347\sqrt[3]{P}}\right]^{1.8127} \quad (4)$$

It is possible to improve Equation 4 by calibrating the near-source term using the method from McGarr (1991) on a subset of large shear-type sources recorded around the mine. The obtained PGV_0 values were approximated by a log-normal distribution with a mean PGV value of 0.252 m/s and $\sigma_{\text{logPGV}} = 0.468$ m/s (Figure 6). For specific scenarios, the GMPE constants in equation 1 can be modified using an estimate of the near fault PGV from McGarr (1991). The equation and associated uncertainty, σ_{logPGV}, can be used in a conventional probabilistic ground motion hazard assessment for planned mining. In this work we apply the equation in a deterministic sense, for a retrospective assessment of shaking intensity from a specific historical large event. For this application we adjust the near-source term of the equation, PGV_0, based on measurements for the analysed event. This is demonstrated in the next section.

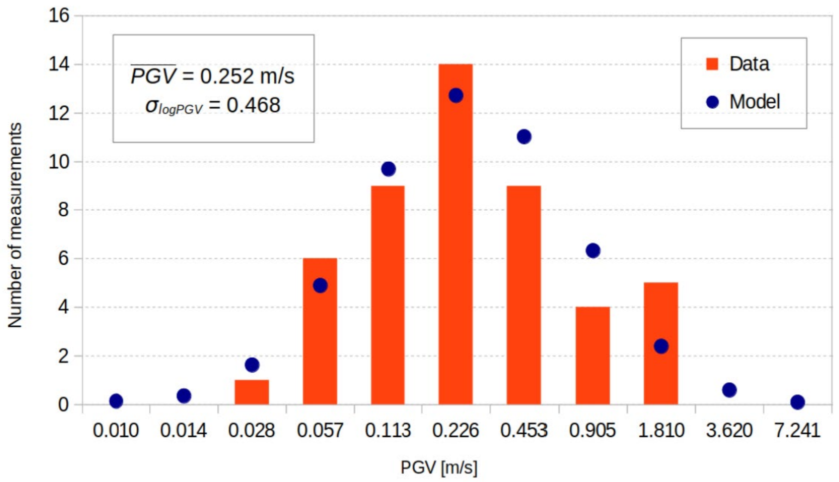

Figure 6 Distribution of near-source PGV_0 estimates for different large shear-type sources at Oyu Tolgoi (after Malovichko 2023a). The values along the X-axis represent the central binned velocities

2.2 Strainburst damage mechanism and bulking velocity

Table 4 summarises the differences in approach to 2 main types of seismically induced damage observed in deep underground mines. If a damaging seismic event has a crush-type mechanism and occurs in a straight tunnel (simplest case), then the following steps may be followed:

- Estimate depth of strainbursting, d_{SB}, from the scalar moment (or potency) of seismic events considering the far-field stress, Poisson's ratio and geometrical characteristics of the tunnel as described by Malovichko (2023b).
- Estimate the bulking duration, t_{SB}, from the duration of P-wave and S-wave pulses as described by Malovichko (2023b).
- Estimate an appropriate bulking factor, BF, based on extensometer or lidar measurements.

The bulking or strainbursting velocity is then estimated as follows (Kaiser & Malovichko 2022):

$$V_{SB} = \frac{BF d_{SB}}{t_{SB}} \tag{5}$$

Table 4 Summary of shaking and bulking ground velocities assessment

Shakedown	Strainbursting
Required input: Source size (magnitude, seismic potency, seismic energy) Distance to the source GMPE	Required input: Depth of strainbursting Bulking duration BF
Output: PGV and its uncertainty	Output: V_{SB} and its uncertainty
Limitations: Applicable for slip-type events, for which GMPE is typically calibrated	Limitations: Applicable for straight parts of tunnels For large or distributed seismic events, the parameters of slip- and crush-type subsources must be reconstructed using finite source inversion (Malovichko et al. 2025)

3 Results

3.1 Seismological analysis

Routine moment tensor analysis is possible at most mines with sufficient sensor density and coverage. At Oyu Tolgoi, moment tensors are automatically evaluated using either a full-waveform (FW) inversion or a polarities and amplitudes approach. For all events with reliable hypocentre and magnitude estimates recorded since 1 January 2021, approximately 24% have moment tensor solutions; however, for significant seismic events (M_W ≥0.5) the percentage is 97.5%. By assessing the source type first (demonstrated in Figure 7), the mine can follow appropriate guidelines to estimate the demand placed on ground support systems.

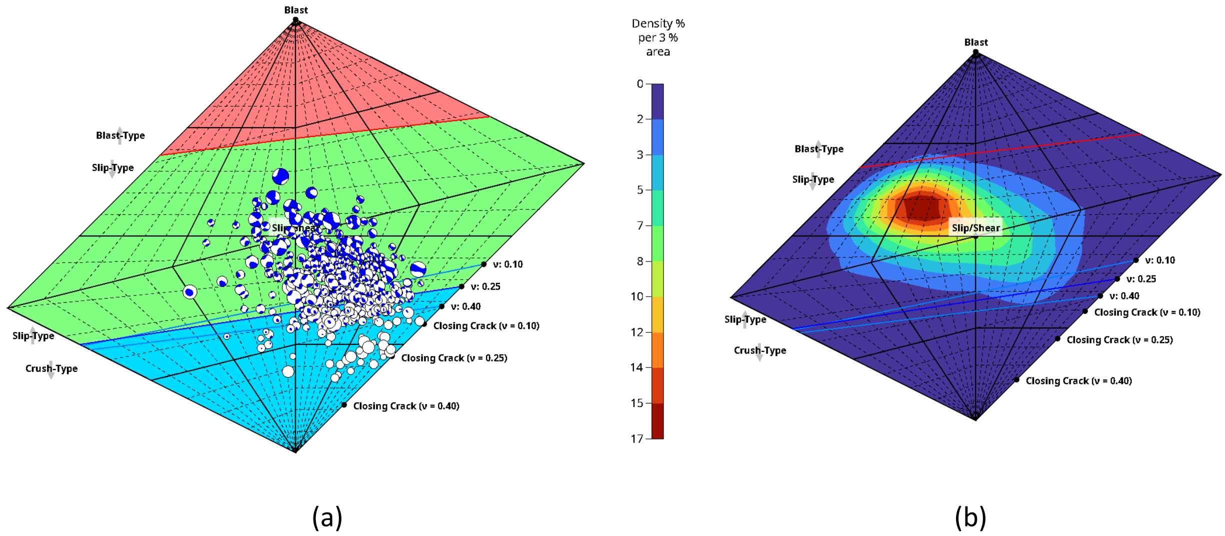

Figure 7 (a) Distribution of source types for events with M_W ≥0.5; (b) Available moment tensors (more than 82,000)

Three significant seismic events were selected for further analysis as discussed in the following subsections: a predominantly shear-type source and 2 crush-type sources.

3.1.1 *Case 1: M_W 2.0 shear-type source*

For this event, the FW inversion (Butterworth bandpass filter 3–8 Hz) method yielded an oblique strike-slip solution as depicted in Figure 8. Based on this and accurate estimates of the event hypocentre and seismic potency, the expected shaking (PGV) can be calculated for any point in space using the GMPE calibrated for Oyu Tolgoi (Malovichko 2023a).The estimated corner frequency was 8.4 Hz with a static stress drop of 0.24 MPa; therefore, according to Brune et al. (1979), the estimated source radius is 112 m. Considering the event hypocentre (estimate of location of initiation) was less than 150 m from the nearest tunnel, the tunnels may have actually been in the near-fault domain. It is therefore reasonable to consider an estimate of $\overline{PGV_0}$ for an estimate of shaking intensity at the nearest excavations. The method of McGarr (1991) was used where the peak ground accelerations were from the instrument corrected, low-pass 100 Hz filtered seismograms (Figure 8). The constants required for Equation 2 (rigidity, S-wave velocity and density) were assumed based on available data for Oyu Tolgoi and, using an assumed constant attenuation, $Q_{(P=S)}$, and approximated dominant period, T_{dom}, (Table 5), we were able to estimate PGV_0.at

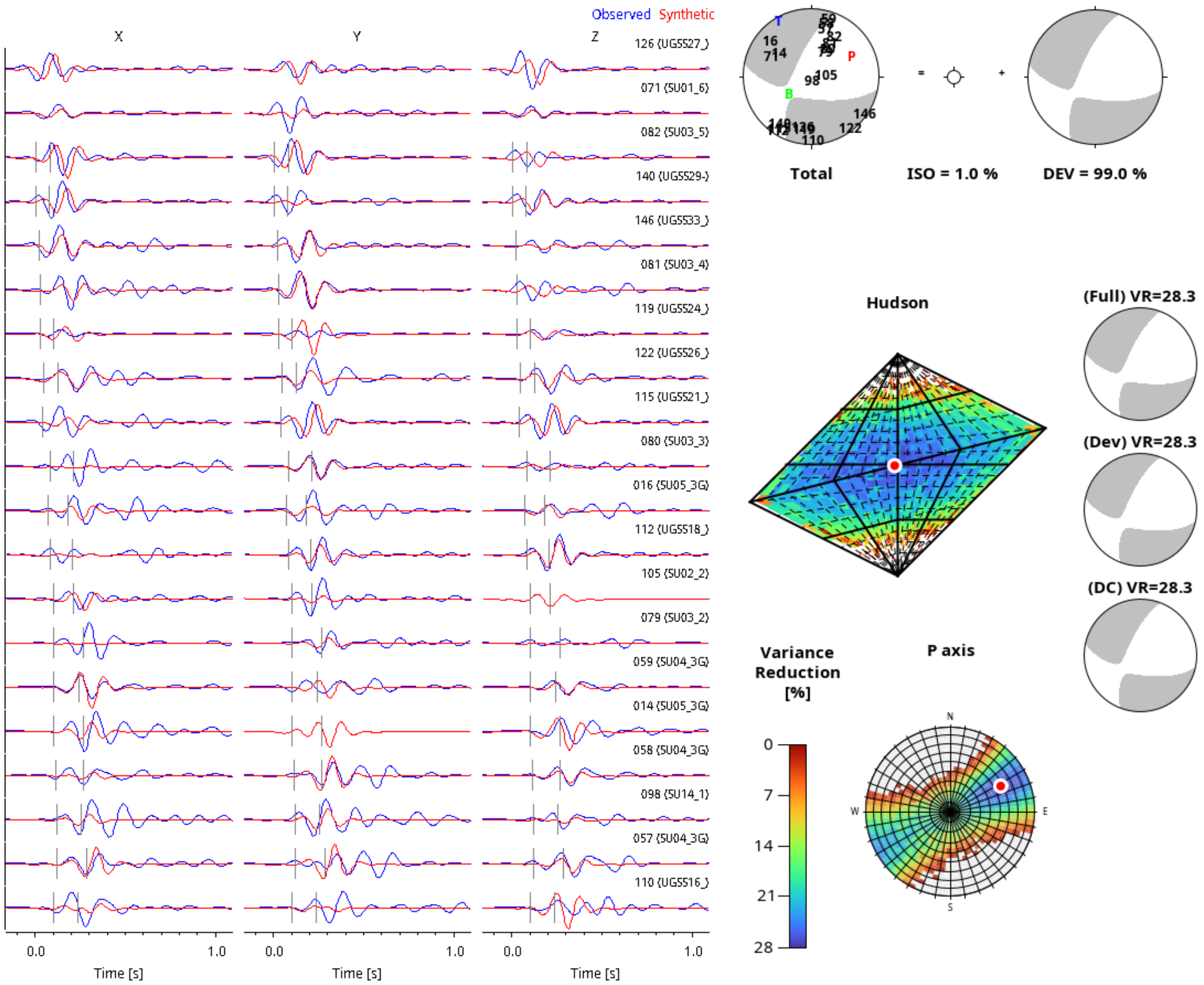

Figure 8 **Result of FW inversion showing the decomposition into isotropic and deviatoric parts for the M_W 2.0 event and associated uncertainty**

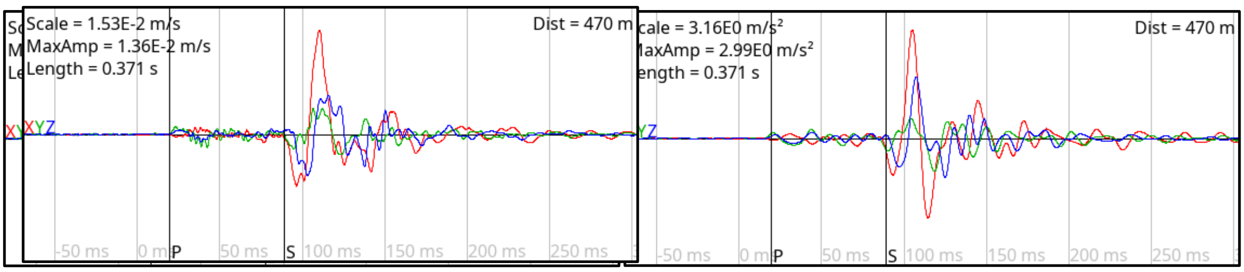

Figure 9 **(a) Example of velocity waveform data versus low-pass 100 Hz filtered acceleration data; (b) Example of velocity waveform data from Sensor 140. These waveforms were used to estimate the slip velocity and corresponding near-fault PGV**

Table 5 Results of near-fault PGV estimates using the method of McGarr (1991) for seven nearest triaxial geophone recordings of the M_W 2.0 event

Constants for Equation 2: μ = 25.9 GPa, β = 3,100 m/s, ρ = 2,700 kg/m^3, Q_P = Q_S = 300, T_{dom} = 0.035 s				
Site	R **(m)**	PGA **(m/s^2)**	$\dot{D}$ **(m/s)**	PGV_0**(m/s)**
126	401	1.93	0.66	0.33
82	462	1.94	0.77	0.39
140	470	2.99	1.21	0.61
101	503	3.12	1.36	0.68
70	521	2.14	0.97	0.48
115	653	1.39	0.80	0.40
112	815	0.77	0.56	0.28
		$\overline{PGV_0}$		0.510

For points of interest or locations where shakedown is observed, the near-source term in the GMPE can be aligned with the estimate of $\overline{PGV_0}$ by effectively shifting the PGV-Distance curve to better match the nature of the slip. In this case, the adjusted GMPE becomes:

$$\overline{PGV} = 0.510\left[\frac{22.347\sqrt[3]{P}}{R+22.347\sqrt[3]{P}}\right]^{1.8127} \tag{6}$$

3.1.2 *Case 2: M_W 1.3 and M_W 1.4 crush-type sources*

An example of a bulking velocity estimation was conducted for 2 large crush-type sources that occurred approximately 3 minutes and 30 seconds apart with magnitude estimates of M_W 1.3 and M_W 1.4, respectively. Both events were located in a region of complex tunnel geometry subjected to elevated abutment stresses from the P0 cave. The hypocentre of the M_W 1.3 event co-locates with an area of shotcrete ejection in the shoulder of an undercut level drive. Lidar scanning provided an estimated depth and extent of failure as shown in Figure 10.

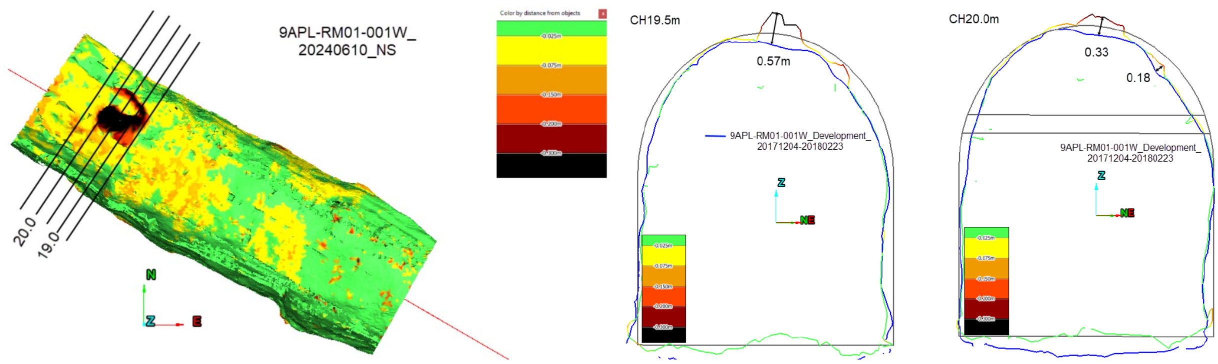

Figure 10 Lidar scan results along a damaged section of tunnel following the M_W 1.3 and M_W 1.4 events

Analysis of the waveform data from the M_W 1.3 event yields an approximate bulking duration, $t_{SB} = 0.032$ s. The moment tensor solution and associated uncertainty for the M_W 1.3 event is presented in Figure 11. To match the low-frequency part of the source (below corner frequency of the source), the waveforms were bandpass-filtered between 3 and 20 Hz prior to the inversion. Following the approach of Kaiser & Malovichko (2022) and Malovichko (2023b), we can estimate a total depth of strainbursting and bulking velocity provided we have a reasonable estimate of the BF. If required, the BF can be calibrated using lidar scans before and after seismic events and estimates of the depth of strainbursting for selected damaging events along tunnels.

Ideally, there should be no ejection of material prior to the post-seismic event lidar scan so that displacement (bulking) along the surface of the tunnel can be accurately measured. The depth of strainbursting along a tunnel can be calculated from the scalar seismic moment of a crush-type source and estimates of the maximum in-plane stress, $\sigma_{\max}$, tunnel diameter, L_A, Poisson's ratio, ν, and an assumed ratio of the depth to length of failure along the tunnel, R. The results of the lidar scan (Figure 10) after the event suggest that damage was distributed along a 10 m section of tunnel with a maximum depth of 0.6 m. This gives $R \approx 0.06$. By applying a BF, we can estimate the amount of displacement that occurred on the surface of the tunnel and finally from our estimate of bulking duration, $t_{SB} = 0.032s$, we can estimate V_{SB}. For demonstration purposes, the value for BF had to be assumed but a more rigorous approach is to calibrate this parameter using lidar scan data and past seismic events. An estimate of $\sigma_{\max}$ was made from available stress modelling results. Results for the M_W 1.3 event are presented in Table 6.

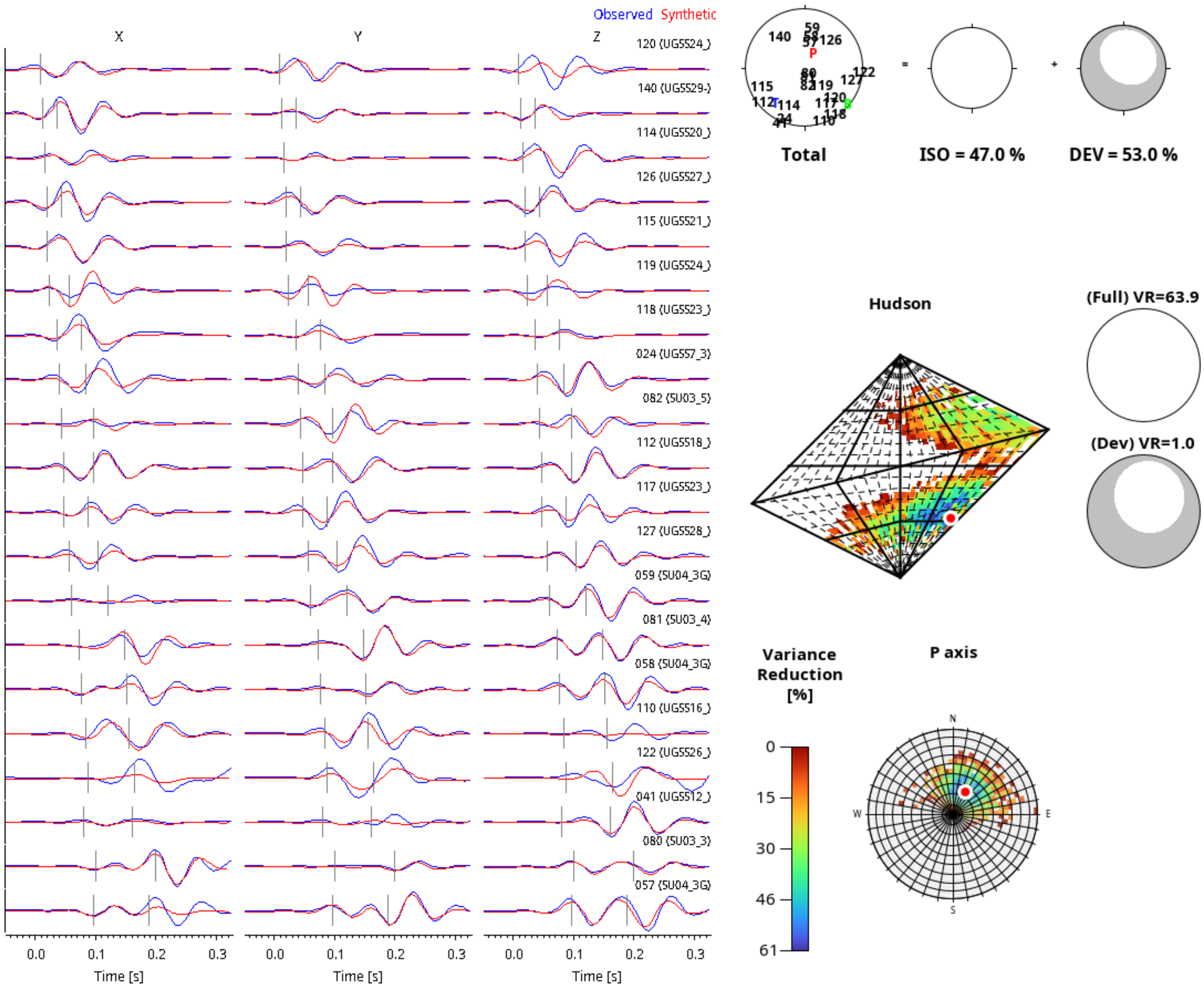

Figure 11 Result of the FW inversion showing the decomposition into isotropic and deviatoric parts for the M_W 1.3 event and associated uncertainty

Table 6 Calculation of bulking velocity for the M_W 1.3 seismic event

Scalar seismic moment $\|M\|$	**1.4E + 11 Nm**
Maximum in-plane stress, σ_{max}	60 MPa
$R\left(\Delta\, d_f^{max}/L\,3\right)$ Ratio of depth to length of failure along tunnel	0.06
Effective tunnel diameter, L_A	5.0 m
Poisson's ratio, ν	0.25
Bulking factor, BF	0.03 = 3%
Depth of strainbursting, d_{SB}	1.72 m
Displacement, $u_{SB} = d_{SB} \cdot BF$	0.05 m
Velocity, $V_{SB} = u_{SB}/t_{SB}$	1.61 m/s

3.1.3 Case 3: M_W 1.8 crush-type source with distributed damage

A few months after the 2 events discussed in Case 2, the same area produced an M_W 1.8 crush-type source. In this case damage was more significant and occurred at 3 locations above and below the initiation point. As mentioned in Table 5, for large or distributed seismic events, the parameters of slip- and crush-type subsources must be reconstructed using finite source inversion. A finite source scenario was constructed with *a priori* assumptions about the direction of loading, duration and spatial extent of the event and the initiation point. These assumptions are informed by an initial moment tensor solution using the point source approximation, an estimate of the initiation point, and associated uncertainty and damage observations (Figure 12). Details of the method can be found in Malovichko et al. (2025).

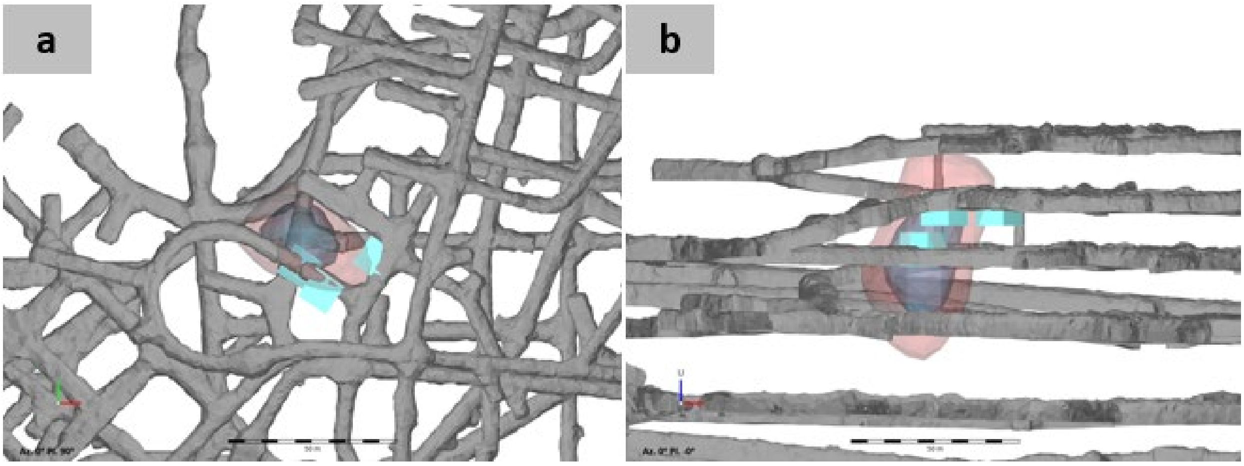

Figure 12 Complex tunnel geometry around the initiation points of an M_W 1.8 crush-type source. (a) Plan view; (b) View looking north. The blue boxes mark locations of lower wall ejection and bulking in the upper drive and bulking in the shoulder of the lower drive. The dark blue and red iso-surfaces represent 68% and 95% confidence regions for the initiation point

The inversion scheme allows the source to evolve in space and time while trying to fit the high-frequency part of the signal, in this case up to 50 Hz. This is because higher frequency signals are sensitive to small-scale variations (~10 m) in the locations and origin times subsources. Based on the damage observations, 3 crush-type subsources were assumed, each 10 × 10 m in size.

The obtained solution in terms of cumulative convergence and convergence rate at the 3 damage locations is presented in Figure 13. Figure 14 shows the resulting waveform fit. The misfit using variance reduction was 43.1% and the cumulative potency from the finite source (23.6 m^3) compared well with that from the point source estimate (21.7 m^3). The most significant damage occurred in the upper drive (northernmost box in Figure 13), which matched the location of largest convergence from the finite source inversion in Figure 14.

It should be kept in mind that the ejection of material does not contribute to the radiation of seismic waves and the convergence that is estimated here can be both inelastic and elastic. The rate of convergence describes the movement of both walls, i.e. each wall moved at half the rate given in Figure 14.

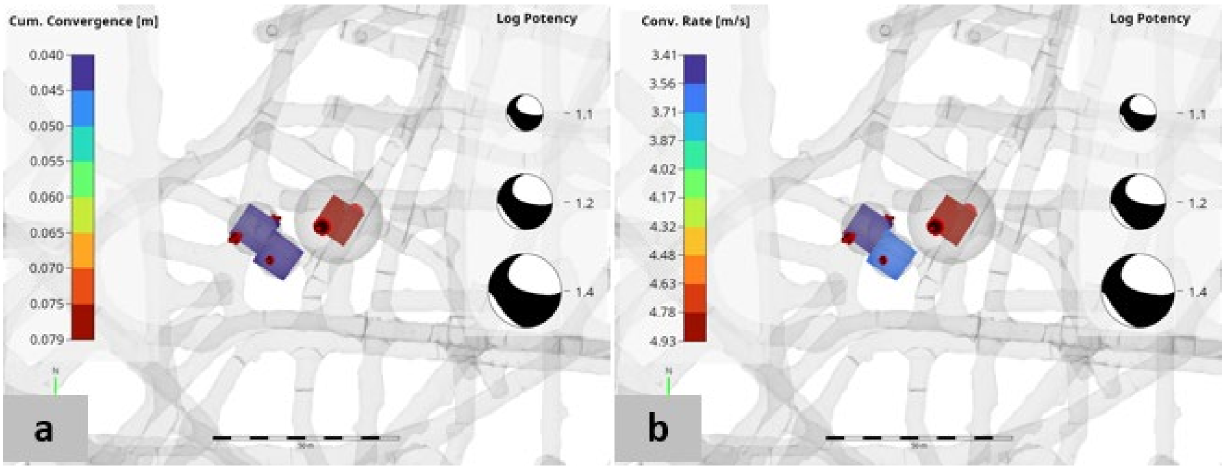

Figure 13 (a) Cumulative convergence; (b) Rate of convergence at the 3 damage locations associated with the M_W 1.8 event

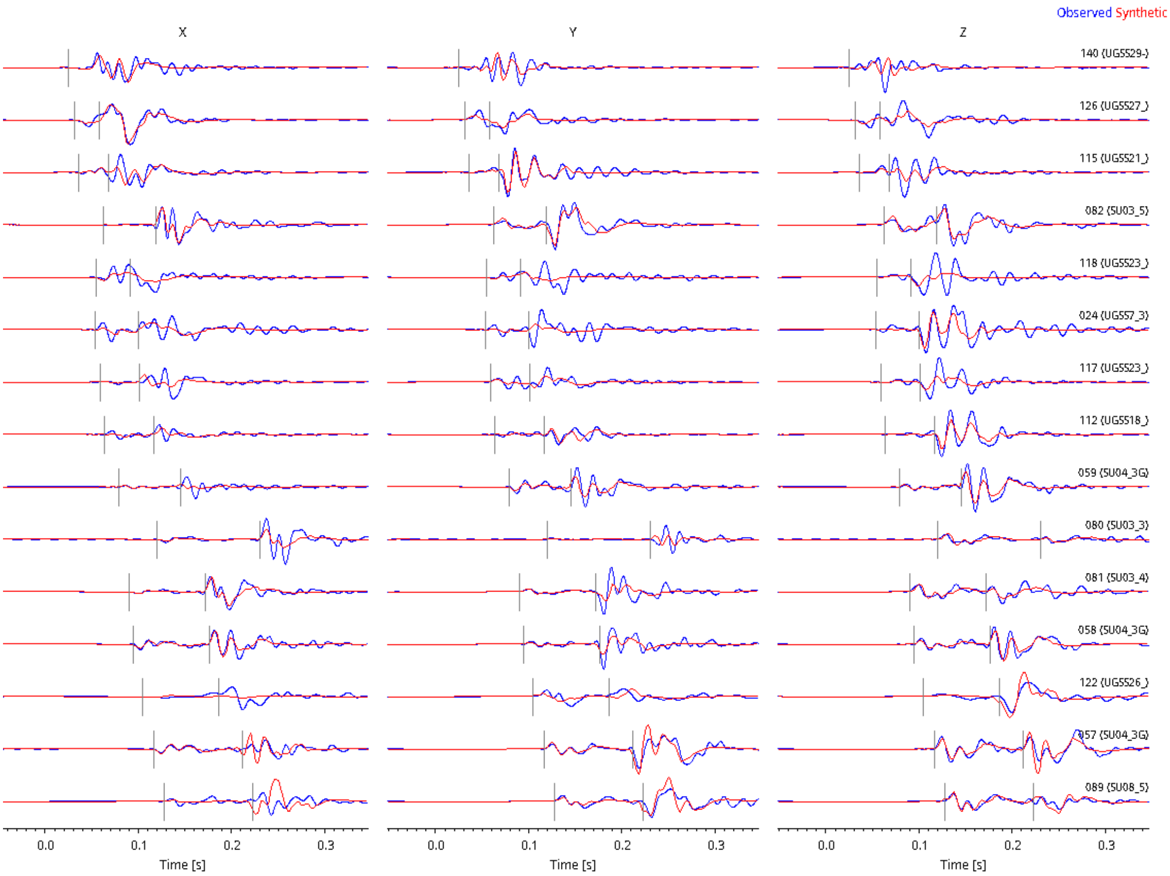

Figure 14 Fit of observed waveform data (blue) with waveform data from the modelled finite source (red) overlaid. A bandpass filter (5–50 Hz) was applied prior to the inversion in order to resolve features of the smaller (10 m) subsources

Although this is not considered rigorous, the approach demonstrated in Section 3.12 for straight tunnels can be applied independently for the 3 inverted subsources to estimate the depth of strainbursting and the bulking velocity. Each subsource is assigned a seismic moment and bulking duration from the results of the inversion. Figure 15 summarises the results for d_{SB} and V_{SB} for each subsource. The tunnel dimensions and characteristics of the observed damage were similar to Case 2; therefore, values for L_A, σ_{max}, ν and R were taken from Table 7.

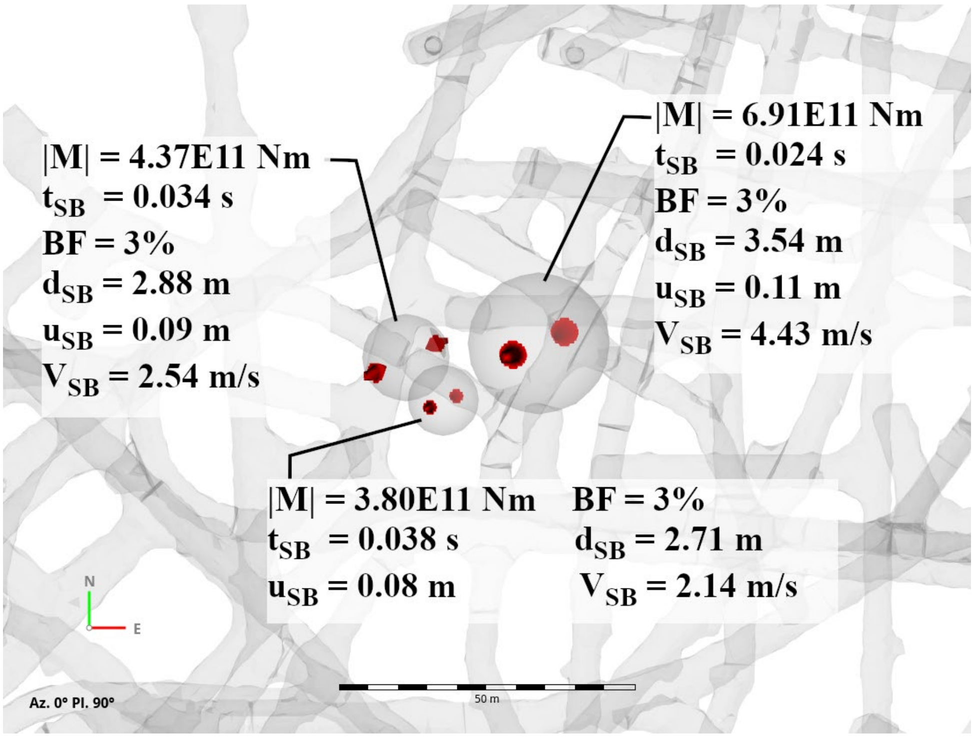

Figure 15 Summary of d_{SB} and V_{SB} estimates calculated for each subsource of the M_W1.8 event. Here the subsources are plotted in plan view of the affected area

The result may be considered a conservative estimate, since we only assigned subsources to locations where damage was observed. Part of the seismic radiation may originate from other sections of tunnel where no damage was observed.

4 Conclusion

This study presents a structured approach for estimating the main input parameters (PGV and V_{SB}) to inform calculation of the demand on the excavation support elements from seismic events with the appropriate considerations. Routine moment tensor analysis, which is a common feature of many seismic systems monitoring underground mines, forms the foundation for assessing the seismic source type and selecting the appropriate method to estimate the amount of the dynamic loading. The paper demonstrates how estimates for V_{SB} are often orders of magnitude larger than PGV and therefore should be considered as part of a thorough back-analysis of large seismic events. The classification of seismic events into shear and crush types offers valuable insights into potential damage mechanisms, such as ground support element ejection, wall failure or shakedown of unsupported/compromised ground, thus enabling targeted hazard management strategies to be developed. One example of proposed integration into the seismic hazard management plan is to regularly assess support consumption (depth of failure) from crush-type sources around the mine, thereby facilitating proactive mitigation measures. The comparison of seismic data with geotechnical observations highlights the reliability and relevance of these methods. Effectively linking seismic event classification to dynamic loading parameters, this study bridges the gap between theoretical analyses and practical applications in ground management. Further refinements to the estimates of V_{SB} are possible with more accurate stress modelling results (validated against observations) and regular lidar scans before and after large seismic events.

Acknowledgement

The methods in this study were made possible by comprehensive datasets and geotechnical observations. We extend our gratitude to our partners and collaborators for their valuable insights and contributions.

References

Brune, JN, Archuleta, RJ & Hartzell, S 1979, 'Far-field S-wave spectra, corner frequencies, and pulse shapes', *Journal of Geophysical Research*, vol. 84, no.B5, pp. 2262–2272, https://doi:10.1029/JB084iB05p02262

Kaiser, P & Moss, A 2022, 'Deformation-based support design for highly stressed ground with a focus on rockburst damage mitigation', *Journal of Rock Mechanics and Geotechnical Engineering*, vol. 14, no. 1, pp. 50–66.

Kaiser, PK & Malovichko, DA 2022, 'Energy and displacement demands imposed on rock support by strainburst damage mechanisms', in M Diederichs (ed), *Proceedings of the 10th International Symposium on Rockbursts and Seismicity in Mines*, Society for Mining, Metallurgy & Exploration, Englewood.

Malovichko, D 2023a, *Oyu Tolgoi: Probabilistic assessment of ground motion hazard for underground infrastructure*, internal report OT-REP-PSHA-202303-DMv1.

Malovichko, D 2023b, 'Utilisation of seismic data in the assessment of displacement and energy demand imposed on ground support by strainbursts', in J Wesseloo (ed.), *Ground Support 2023: Proceedings of the 10th International Conference on Ground Support in Mining*, Australian Centre for Geomechanics, Perth, pp. 181–196, https://doi.org/10.36487/ACG_repo/2325_12

Malovichko, D, Rigby, A, Jessu, K & Viegas, G 2024, 'Forecasting shaking and bulking ground velocities around tunnels for a planned mining sequence', in P Andrieux & D Cumming-Potvin (eds), *Deep Mining 2024: Proceedings of the 10th International Conference on Deep and High Stress Mining*, Australian Centre for Geomechanics, Perth, pp. 687-698, https://doi.org/10.36487/ACG_repo/2465_42

Malovichko, D, Jaimes, A & Lotter, E 2025, 'Finite seismic sources in mines: Inversion and utilisation', *Proceedings of the 11th Symposium on Rockbursts and Seismicity in Mines (RaSiM11)*, Luleå University of Technology, Luleå.

McGarr, A 1991 'Observations constraining near-source ground motion estimated from locally recorded seismograms', *Journal of Geophysical Research*, vol. 96, no. B10, pp. 16,495–16,508.

Mendecki, AJ 2019, 'Simple GMPE for underground mines', *Acta Geophysica*, vol. 67, pp. 837–847.

SRK Consulting, 2022, *OT Geotechnical Characterisation – P0 Dominant Rock Mass Properties, R_01-1092-02_SRK_RTINTO*, Vancouver.

Voulgaris, P, Lee, MF & Mollison, LJ 2006, 'Estimation of rock stresses at Oyu Tolgoi, Mongolia', *In-Situ Rock Stress*, Taylor & Francis/Balkema, Michigan.